Supplementary Information

# Near-infrared photothermal conversion of polyoxometalate-modified gold nanorods for plasmon-enhanced catalysis

*Gengxin Wang, Xiaofei Chen, Bao Li\*, Lixin Wu\**

State Key Laboratory of Supramolecular Structure and Materials, College of
Chemistry, Jilin University, Changchun 130012, P. R. China.
*E-mail: wulx@jlu.edu.cn; libao@jlu.edu.cn*

## Table of Contents

## S1. Detailed materials

Cetyltrimethylammonium bromide (CTAB), sodium borohydride ($NaBH_4$), Chloroauric acid trihydrate ($HAuCl_4 \cdot 3H_2O$), silver nitrate ($AgNO_3$), ascorbic acid (AA), deuterium reagent ($D_2O$, Chloroform-$d$) used in experimental tests were purchased from Sigma-Aldrich. 2-(Bromoethyl)-trimethylammonium bromide, Potassium thioacetate, $Na_3PW_{12}O_{40}$ were purchased from Aladdin. $Na_5PMo_{10}V_2O_{40}$ ($PMo_{10}V_2$)[1] and $Na_{12}[WZn_3(H_2O)_2(ZnW_9O_{34})_2]$ ($Zn_5W_{19}$)[2] were synthesized according to the literature. The water used in the experiment was doubly distilled water.

## S2. Measurements

Proton nuclear magnetic resonance ($^1H$ NMR) spectra were performed on Bruker AVANCE 500 MHz and Zhongke-Niujin AS 400 MHz spectrometer by using tetramethylsilane (TMS) as internal reference ($\delta = 0$ ppm). The ultraviolet (UV) spectra were recorded on a Varian CARY 50 Probe spectrometer with a 1 cm quartz cell. Fourier transform infrared (FT-IR) spectra were carried out on a Bruker Vertex 80V FT-IR spectrometer. Raman spectra were conducted on a LabRAM HR Evolution spectrometer (HORIBA, Fr). X-ray diffraction (XRD) data are collected on a Rigaku X-ray diffractometer using Cu Kα radiation at a wavelength of 1.542 Å. High resolution transmission electron microscopy (HRTEM) was conducted on JEOL JEM 2010 under an accelerating voltage of 200 kV. Isothermal titration calorimetric (ITC) data were obtained by using MicroCal VPisothermal titration calorimeter (Malvern, UK). The X-ray photoelectron spectroscopy (XPS) spectra are acquired on an ESCALAB-250 spectrometer with a monochromic X-ray source (Al Kα line, 1486.6 eV). Inorganic elemental analysis was performed on a POEMS inductively coupled plasma atomic emission spectrometer (ICP-AES). Dynamic light scattering (DLS) measurements were done using a Zetasizer NanoZS (Malvern Instruments). The high-performance liquid chromatography (HPLC) was performed on a SHIMADZU LC-20A with a chiral OD-H column (4.6 × 250 mm) obtained from Daicel Chemical Industries Ltd. The eluent was n-hexane/ isopropanol (90:10) at a flow rate of 0.5 mL/min. The photothermal experiments are carried out with a 1 W laser lamp (808 nm) as light source.

## S3. Preparation of cationic surface modification agent.

The synthetic route of synthesis of 2-(Mercaptoethyl)-trimethylammonium chloride (M-TA) is adopted according to the following procedures similar to those in publications.[3]
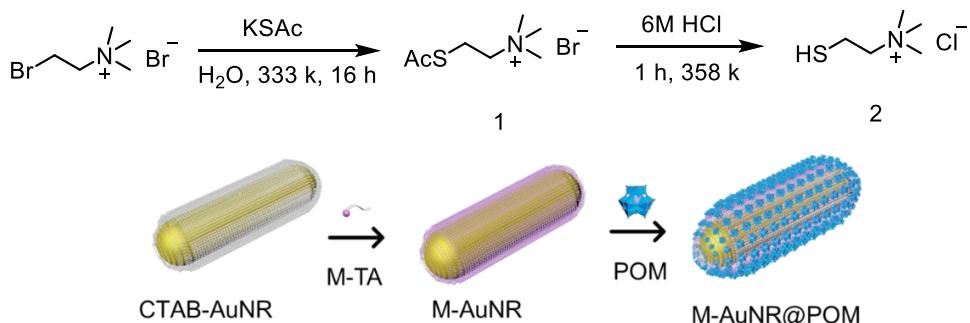


**Fig. S1.** Preparation of surface modification agent M-TA and synthetic route of POM modified AuNRs.

**2-(Acetothioethyl)-trimethylammonium bromide.** 2-(Bromoethyl)-trimethylammonium bromide

(5.00 g, 20.2 mmol) was dissolved in 25 mL $H_2O$ in a round bottom flask. After adding the Potassium thioacetate (3.01 g, 26.3 mmol) to the solution, the mixture was stirred and heated to 60°C for 16 h. Then, the reaction solution was cooled to room temperature, and the solvent was removed under reduced pressure. The residue was purified by repeated extraction and filtration for three times to remove KBr completely. The specific process is as follows. First, the crude product was dissolved in 100 mL MeOH: $CH_2Cl_2$ (1:1) mixing solvent and stirred for 15 min. The resulting mixture solution was filtated to remove KBr. The obtained filtrate was distilled under reduced pressure to remove the solvent and get 4.39 g pure product (90%). 1H NMR (500 MHz, $D_2O$) δ 3.54–3.44 (m, 2H), 3.35–3.27 (m, 2H), 3.21 (s, 9H), 2.44 (s, 3H).

**2-(Mercaptoethyl)-trimethylammonium chloride.** The prepared 2-(acetothioethyl)-trimethylammonium bromide (3.54 g, 14.64 mmol) was dissolved in HCl solution (6 M, 10 mL). Then the solution was stirred and heated to 85°C for 6 h. After this period, the solvent was removed under reduced pressure to get a pale yellow, hygroscopic pure product (2.06 g, 90%). 1H NMR (400 MHz, $D_2O$) δ 3.60–3.46 (m, 2H), 3.15 (s, 9H), 3.01–2.88 (m, 2H). MALDI-TOF MS (m/z): 119.1 $[M^+]$.

**S4. Morphologic and structure characterization of the M-AuNR@POM.**
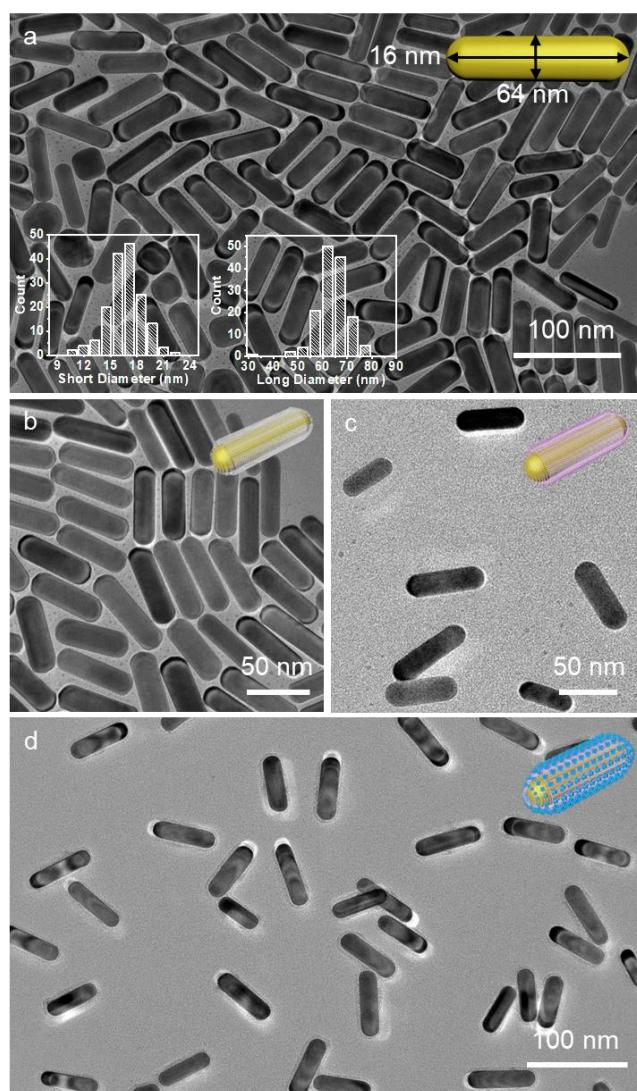


**Fig. S2.** TEM images of (a, b) CTAB-AuNR, (c) M-AuNR and (d) M-AuNR@$PW_{12}$.
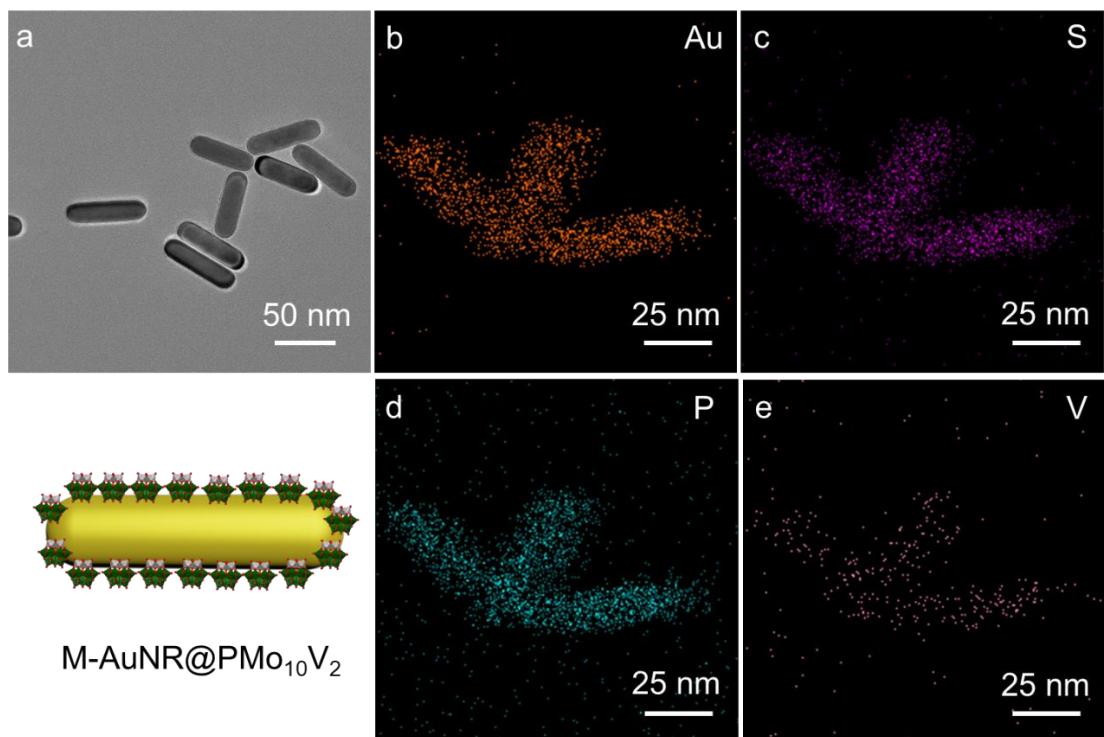
**Fig. S3.** (a) TEM image and schematic drawing of M-AuNR@PMo$_{10}$V$_2$, and (b–e) elemental mappings of M-AuNR@PMo$_{10}$V$_2$.
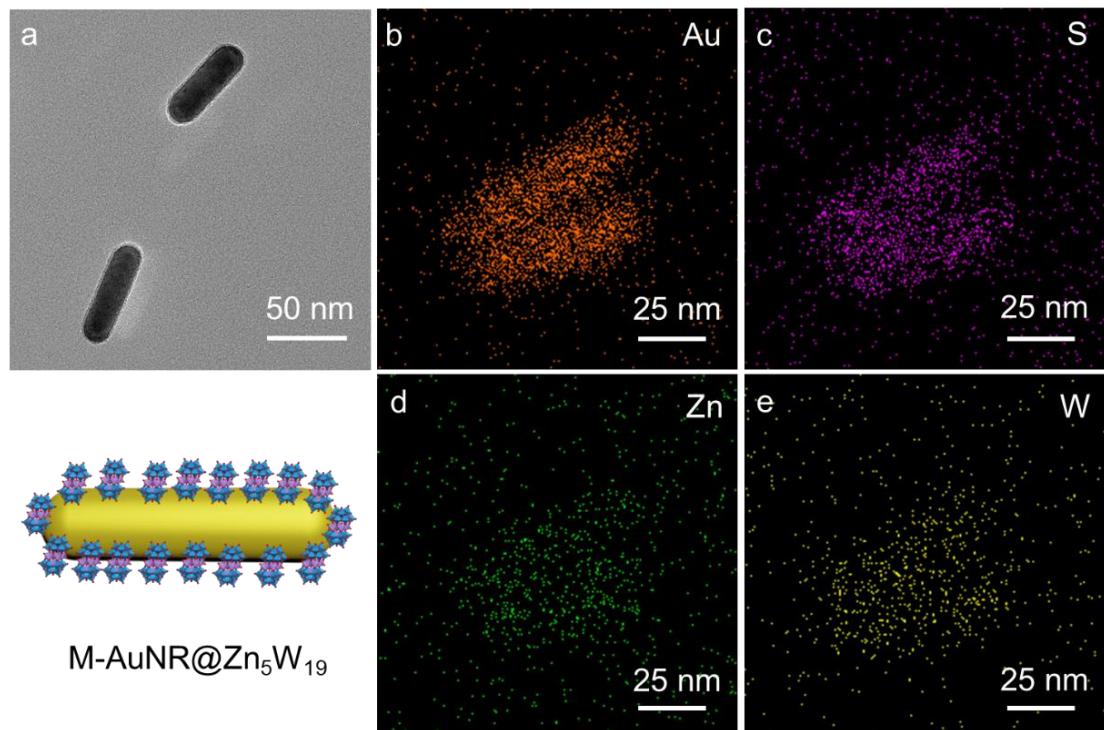


**Fig. S4.** (a) TEM image and schematic of M-AuNR@Zn$_5$W$_{19}$. (b–e) Elemental mapping results of M-AuNR@Zn$_5$W$_{19}$.
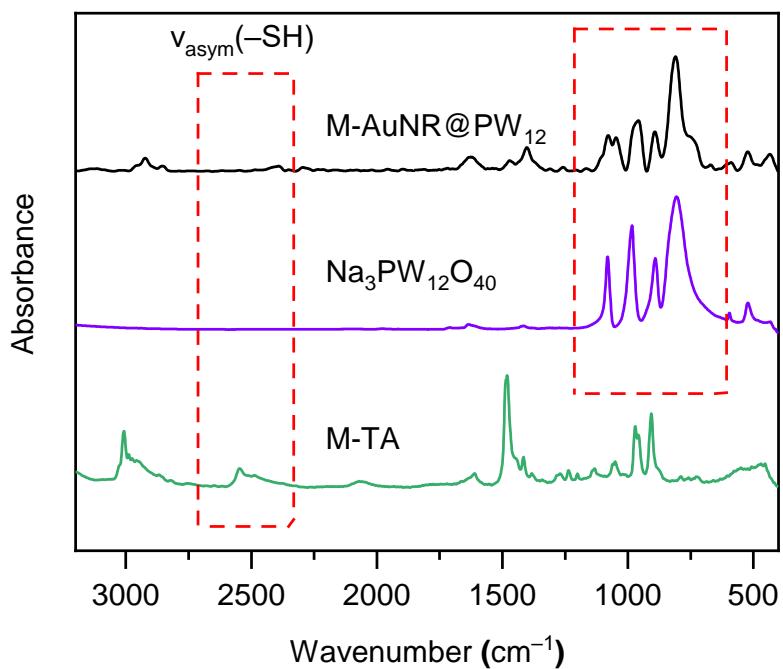
**Fig. S5.** IR spectra of M-AuNR@PW$_{12}$, Na$_3$PW$_{12}$O$_{40}$ and M-TA in KBr pellets.
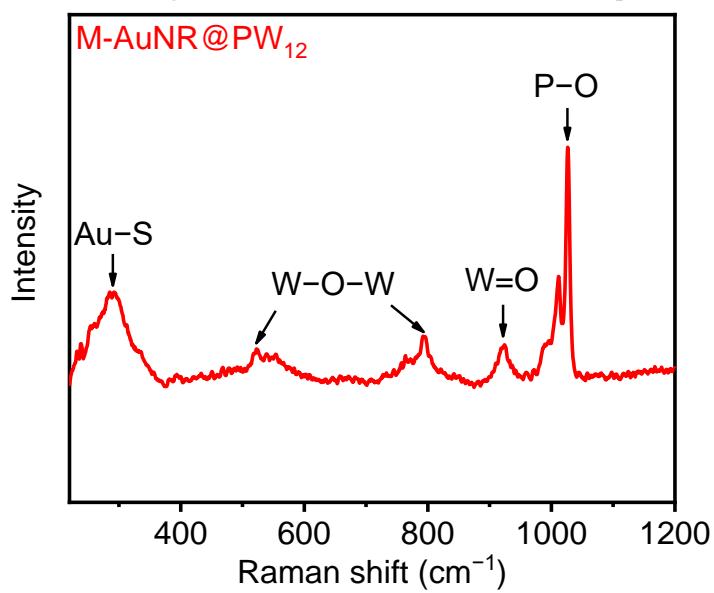


**Fig. S6.** Raman spectra of the M-AuNR@PW$_{12}$ in aqueous solution.
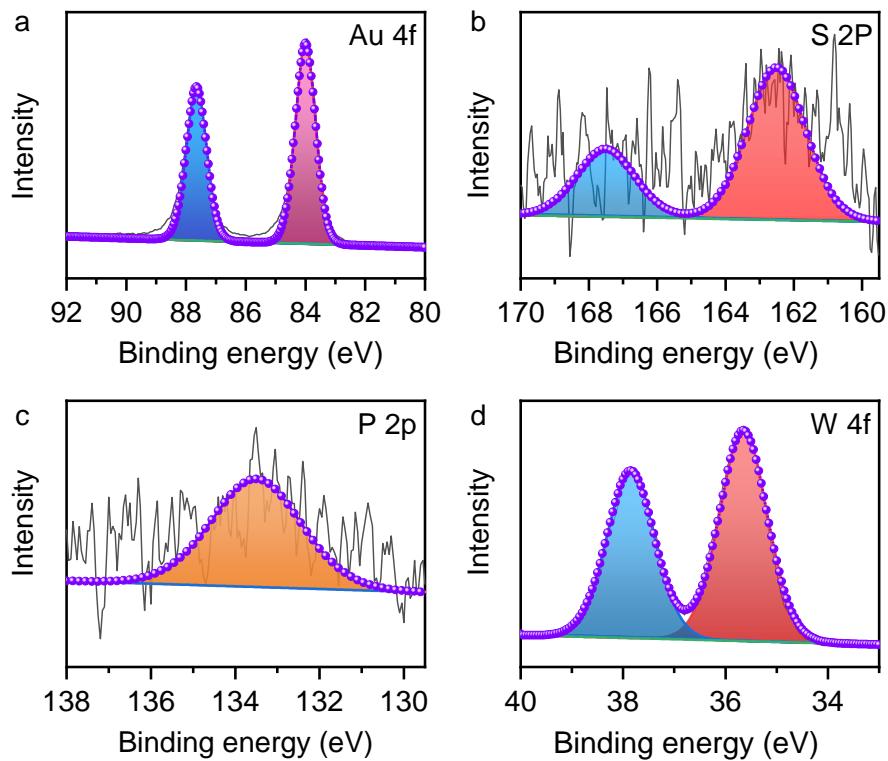
**Fig. S7.** XPS spectra of (a) Au 4f, (b) S 2p, (c) P 2p and (d) W 4f for M-AuNR@PW$_{12}$.
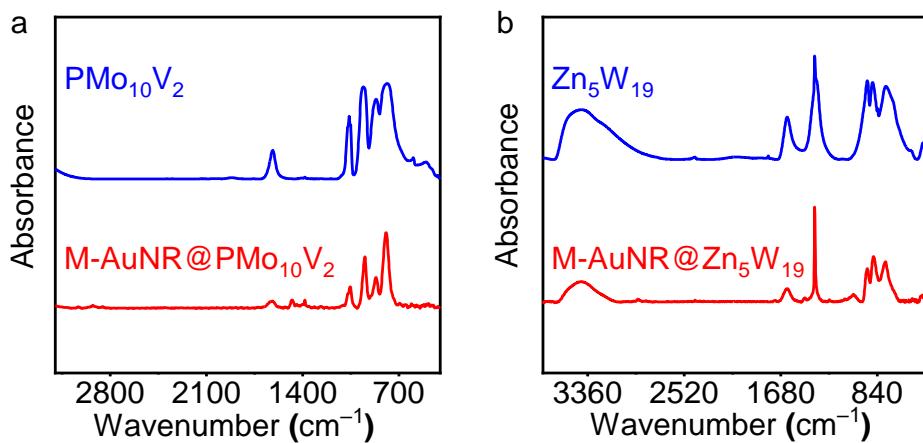


**Fig. S8.** IR spectra of (a) M-AuNR@PMo$_{10}$V$_2$ and (b) M-AuNR@Zn$_5$W$_{19}$ in KBr pellets.
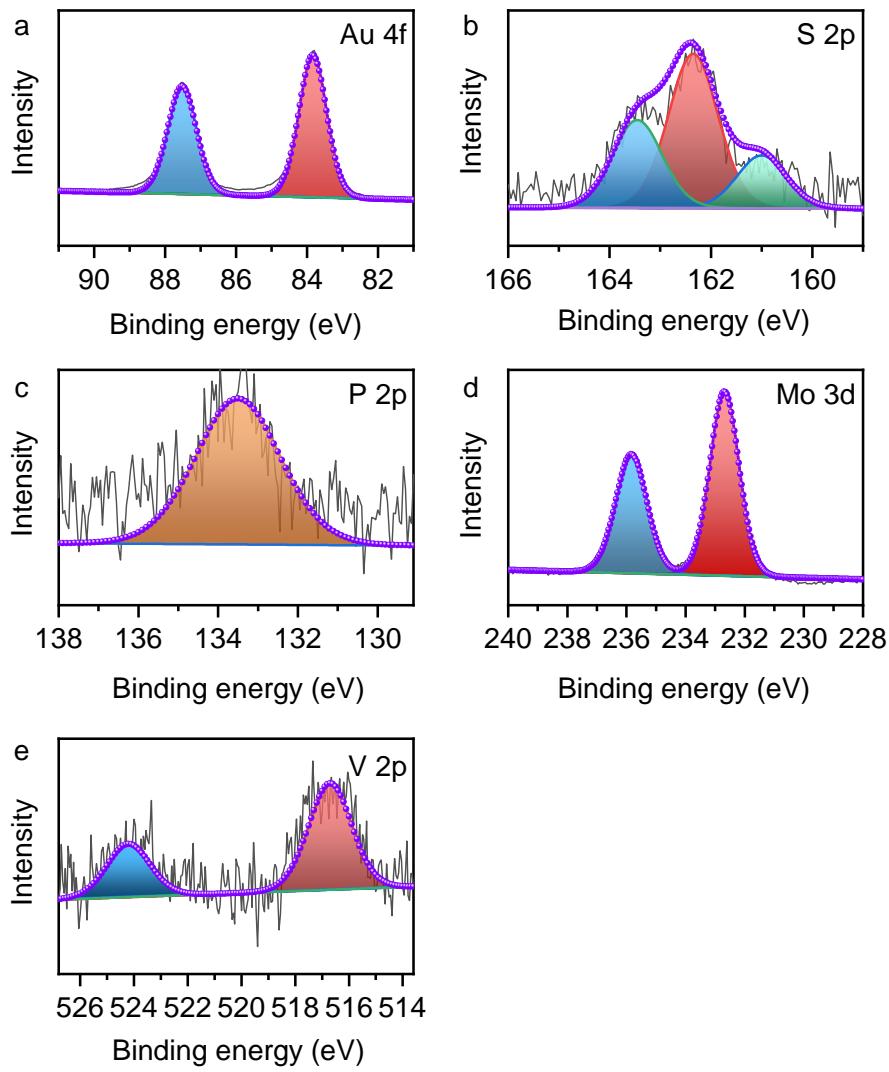
**Fig. S9.** XPS data of (a) Au4f, (b) S2p, (c) P2p, (d) Mo 3d, (e) V2p for M-AuNR@PMo$_{10}$V$_2$.
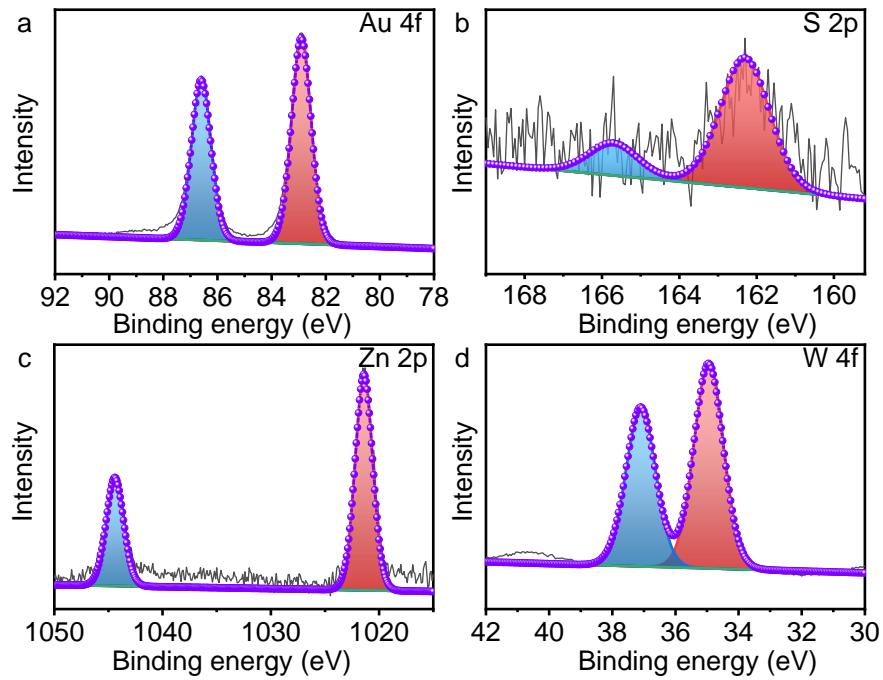


**Fig. S10.** XPS spectra of (a) Au 4f, (b) S 2p, (c) Zn 2p and (d) W 4f for M-AuNR@Zn$_5$W$_{19}$.
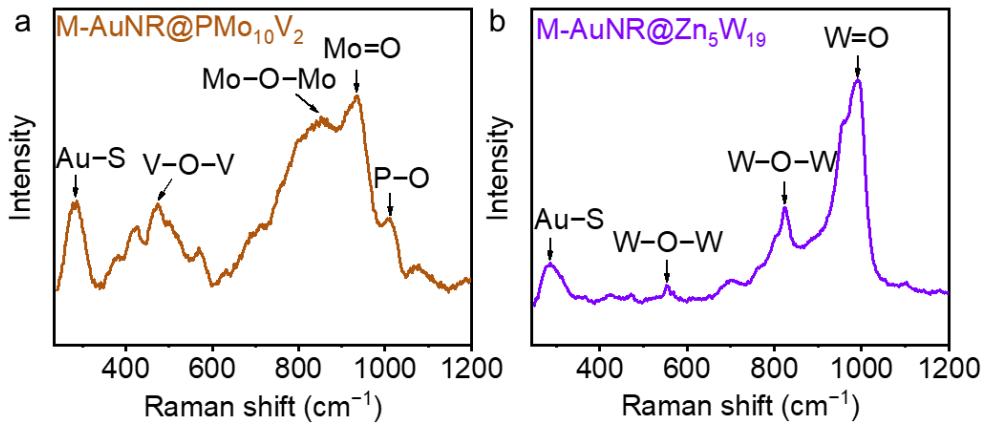
**Fig. S11.** Raman spectra of (a) M-AuNR@ $PMo_{10}V_2$, and (b) M-AuNR@ $Zn_5W_{19}$ in aqueous solution.
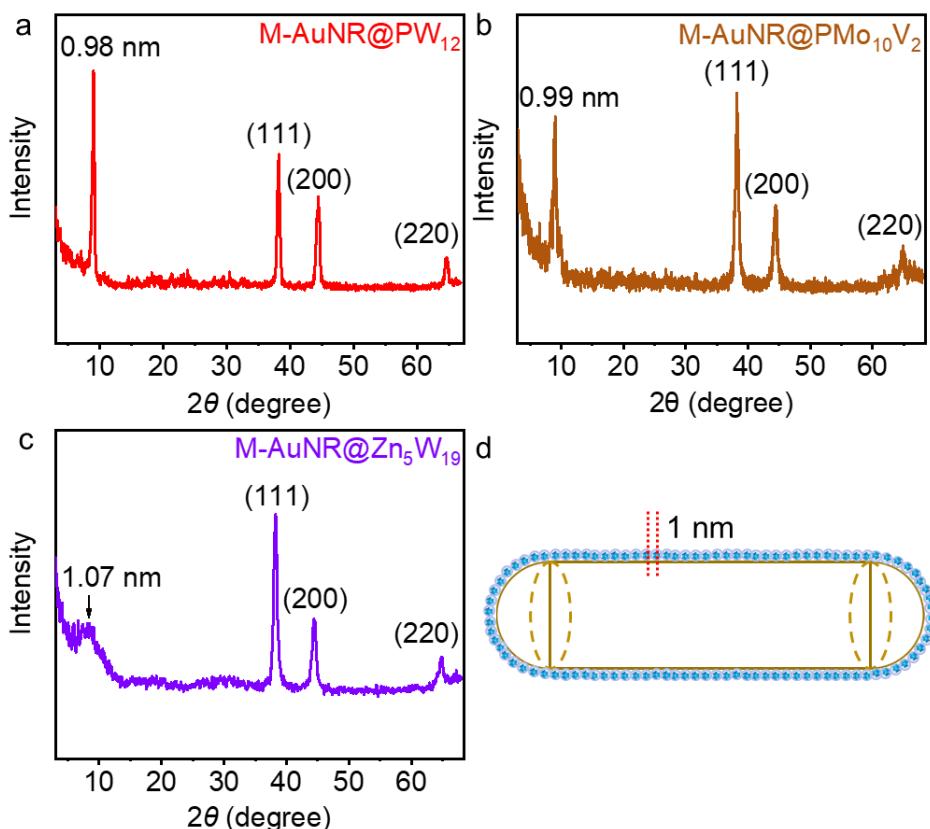


**Fig. S12.** PXRD patterns of (a) M-AuNR@$PW_{12}$, (b) M-AuNR@$PMo_{10}V_2$, and (c) M-AuNR@$Zn_5W_{19}$, and (d) proposed stacking of the longitudinal section of M-AuNR@$PW_{12}$.
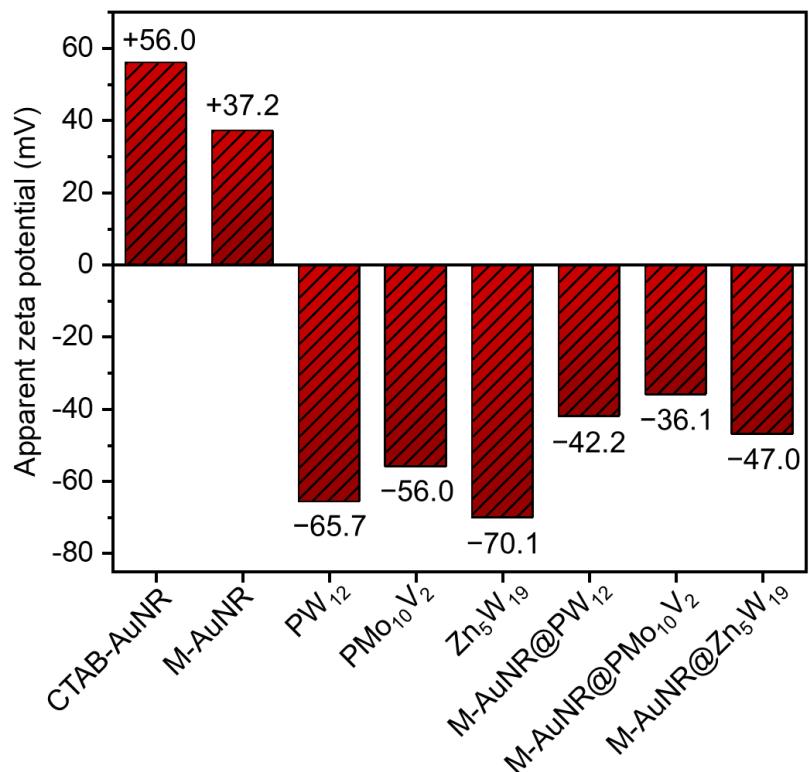
**Fig. S13.** Zeta potential of CTAB-AuNR, M-AuNR and M-AuNR@PW$_{12}$, M-AuNR@PMo$_{10}$V$_2$ and M-AuNR@Zn$_5$W$_{19}$ in water.
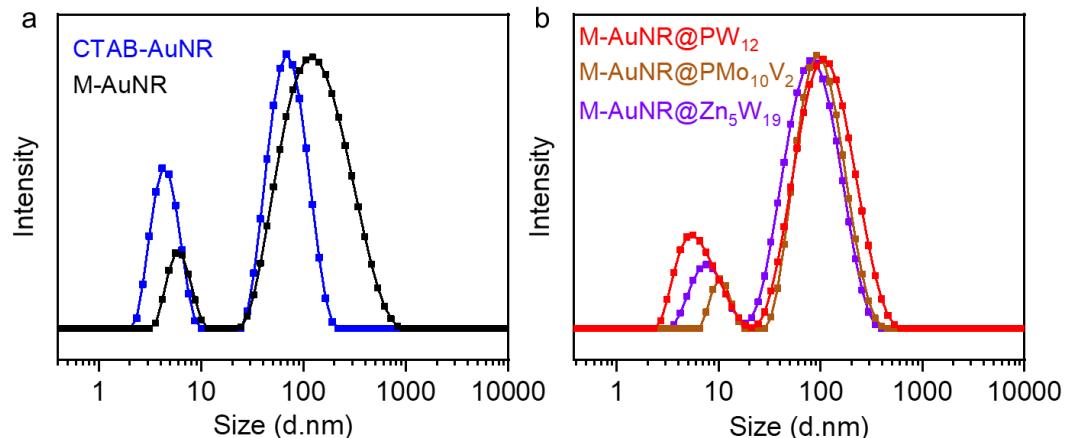


**Fig. S14.** DLS diagrams of (a) CTAB-AuNR, M-AuNR, (b) M-AuNR@PW$_{12}$, M-AuNR@PMo$_{10}$V$_2$ and M-AuNR@Zn$_5$W$_{19}$ in aqueous solution.

## S5. Calculations of POM coverage on AuNR surface.

From the statistics of TEM image shown in Figure S2a, the average length diameter size of AuNR is 64 nm, and the short diameter size is 16 nm. According to the reported results, the structure model of $PW_{12}O_{40}$ cluster can be approximated as a sphere with a diameter of 1 nm. The structures are shown in Fig. S12a and b. In the case of POMs modified on the Au surface to form a fully covered monolayer, the cross-section of M-AuNR@$PW_{12}$ can be drawn in Fig. S12d. Then the specific surface area of M-AuNR@$PW_{12}$ can be obtained. From ICP-MS result, the total mass of Au (0.1356 mg) and $PW_{12}O_{40}$ (0.0199 mg) in 1.0 mL of sample solution. Thus, the total surface area of M-AuNR@$PW_{12}$ and POMs can be calculated. Correspondingly, the coverage of POMs on gold surface can be estimated from the ratio of the total surface area of POMs to the total surface area of M-AuNR@$PW_{12}$. The detailed calculation is shown as follows.
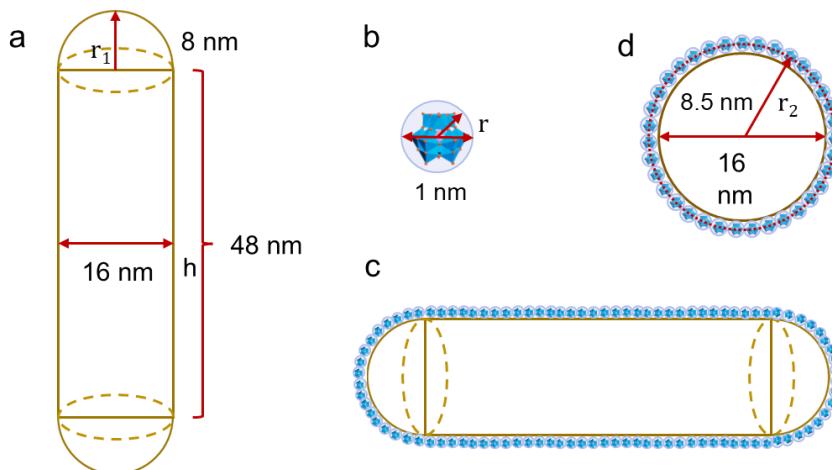


**Fig. S15.** Diagram of structure model of (a) AuNR, (b) $PW_{12}O_{40}$ cluster and the (c) longitudinal section and (d) cross section of M-AuNR@$PW_{12}$.

mass $(AuNR) = 0.1356$ mg;

Since the density $(Au) = 19.32$ g/cm$^3$,

$$\text{volume } (AuNR)_{all} = \frac{\text{mass } (AuNR)}{\text{density } (Au)} = 7.0186 \times 10^{15} \text{ nm}^3$$

As $r_1 = 8$ nm; $h = 48$ nm; $r_2 = 8.5$ nm; $r = 0.5$ nm

For the volume $(AuNR) = \pi r_1^2 h + \frac{4}{3}\pi r_1^3 = 3756.57\pi$ nm$^3$,

$$\text{the surface area } (M\text{-}AuNR@PW_{12}) = 4\pi r_2^2 + 2\pi r_2 h = 1105\pi \text{ nm}^2$$

Thus,

$$\text{specific surface area } (M\text{-}AuNR@PW_{12}) = 0.2942 \text{ nm}^{-1};$$

surface area $(M\text{-}AuNR@PW_{12})_{all} = 0.2942 \times$ volume $(T\text{-}PW_{12}\text{-}AuNR)_{all} = 2.0649 \times 10^{15}$ nm$^2$

molar amount $(PW_{12}O_{40}) = \frac{\text{mass } (PW_{12}O_{40})}{\text{molar mass } (PW_{12}O_{40})} = 4.0402 \times 10^{-9}$ mol

number $(PW_{12}O_{40}) =$ number $(PW_{12}O_{40}) \times N_A = 2.4330 \times 10^{15}$

$$\text{surface area } (PW_{12}O_{40}) = \pi (\frac{d}{2})^2 = 0.25\pi \text{ nm}^2$$

surface area $(PW_{12}O_{40})_{all} =$ number $(PW_{12}O_{40}) \times$ surface area $(PW_{12}O_{40}) = 1.9099 \times 10^{15}$ nm$^2$

Therefore, the coverage of POMs on the surface of Au will be

$$\frac{\text{surface area } (PW_{12}O_{40})_{all}}{surface\ area\ (M-AuNR@PW_{12})_{all}} = 92.5\%$$

And the theoretical number of polyoxometalates on one AuNR:

$$\frac{surface\ area\ (PW_{12}O_{40})}{surface\ area\ (M-AuNR@PW_{12})} = 4420$$
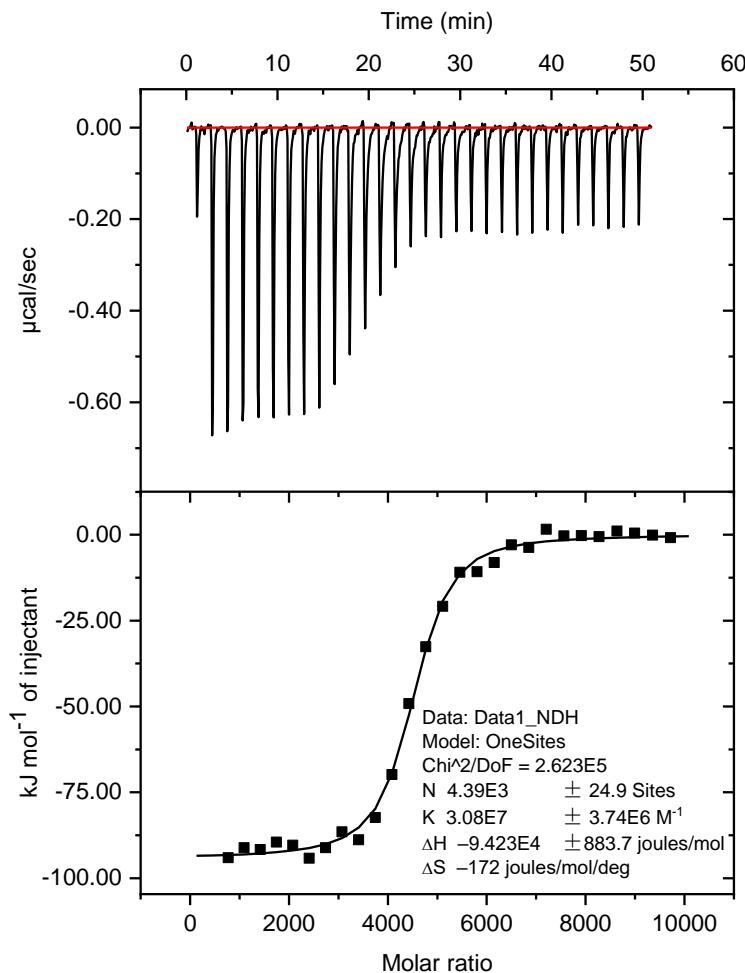


**Fig. S16.** ITC curves and fittings of Na$_3$PW$_{12}$O$_{40}$ (0.0625 mM) titrating M-AuNR (0.097 nM) in water.
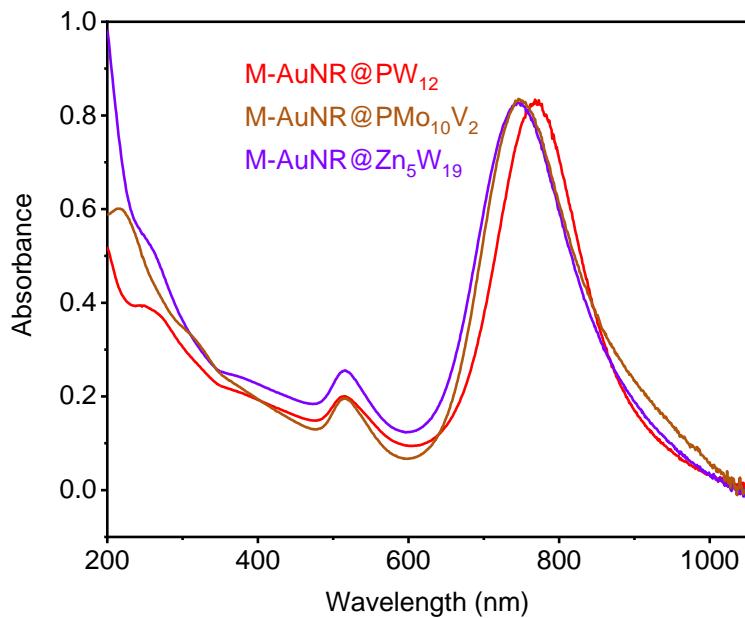
**Fig. S17.** UV-vis spectra of M-AuNR@PW$_{12}$, M-AuNR@PMo$_{10}$V$_2$ and M-AuNR@Zn$_5$W$_{19}$ in aqueous solution.
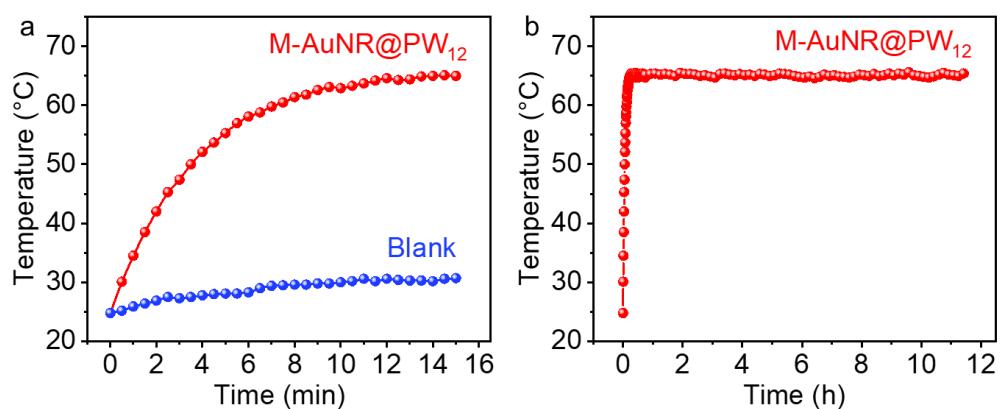


**Fig. S18.** The temperature variation curve of M-AuNR@PW$_{12}$ in aqueous solution under the continuous irradiation of the NIR laser lamp (1.0 W cm$^{-2}$).
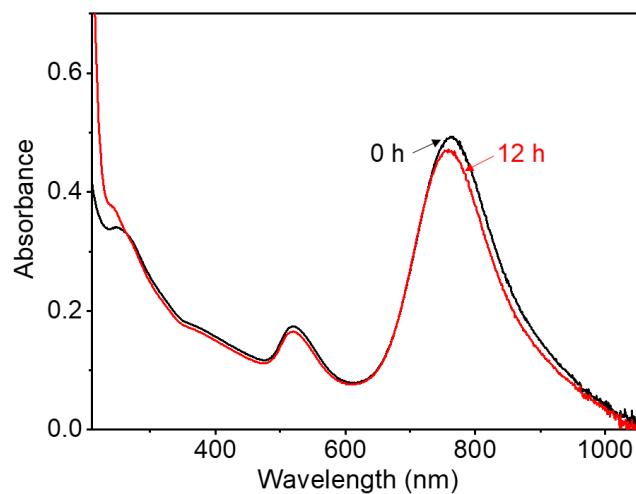


**Fig. S19.** The UV-vis spectra of M-AuNR@PW$_{12}$ aqueous solution after continuous 12 h NIR laser irradiation.

## S6. Photothermal conversion measurements of M-AuNR@POM.

**Calculation of the photothermal conversion efficiency of M-AuNR@PW₁₂.**

1. Calculation of the dimensionless driving force temperature ($\theta$).

$$\theta = \frac{T - T_0}{T_{Max} - T_0}$$

Where $T$ is the solution temperature at time $t$, $T_{max}$ is the highest temperature the solution can reach, $T_0$ is the starting solution temperature.

2. Calculation of the system heat-transfer time constant ($\tau_s$).

$$\tau_S = -\frac{t}{\ln\theta} = 249.71\ s$$

3. Calculation of the value of $hS$.

$$hS = \frac{\sum_i m_i C_{p,i}}{\tau_s} = 0.01682$$

Where $h$ is the heat transfer coefficient, $S$ is the surface area of the container, $m$ is the mass of the water, $Cp$ is the heat capacity of the water.

4. Calculation of the heat released from light absorbed by a container containing pure water ($Q_0$).
$$Q_0 = \frac{cm\Delta T}{t} = 0.02753\ J \cdot s^{-1}$$

Where $\Delta T$ is the temperature drop of the pure water solution after turning off the laser, $t$ is heat dissipation time of pure water.

5. Calculation of the photothermal conversion efficiency ($\eta_{M-AuNR@PW_{12}}$)

$$\eta_{M-AuNR@PW_{12}} = \frac{hS(T_{Max} - T_0) - Q_0}{I(1 - 10^{-A_{808}})} = 78.5\%$$

Where $I$ is the laser lamp power ($I = 1\ W$), $A_{808}$ is the UV absorbance of the solution at 808nm ($A_{808} = 0.755$).
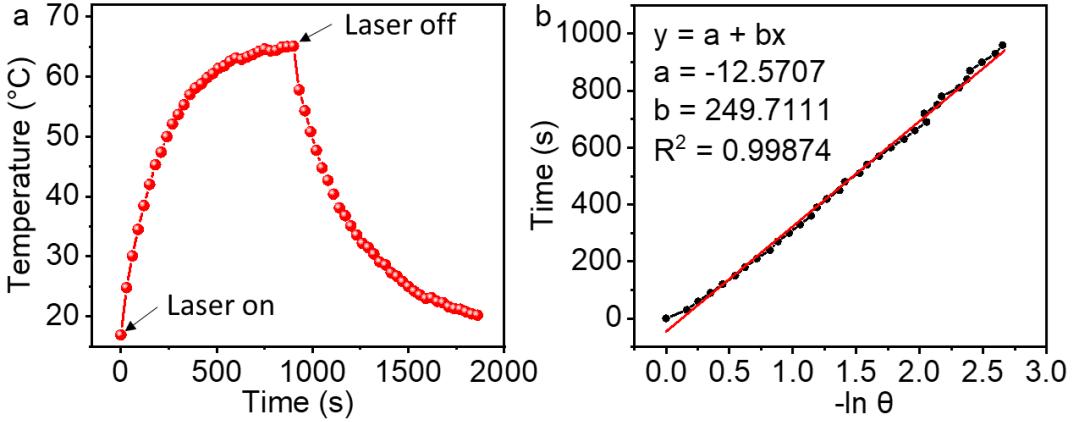
**Fig. S20.** (a) The temperature variation curve of M-AuNR@PW$_{12}$ in aqueous solution: the heating curve is the solution irradiated by the laser lamp (1W cm$^{-2}$), and the cooling process followed happens spontaneously at room temperature after turning off the lamp. (b) The plot of time versus the $-\ln(\theta)$ obtained from the cooling period.

**Calculation of the photothermal conversion efficiency of M-AuNR@PMo$_{10}$V$_2$.**

Calculation of the photothermal conversion efficiency ($\eta_{M-AuNR@PMo_{10}V_2}$)

$$\eta_{M-AuNR@PMo_{10}V_2} = \frac{hS(T_{Max} - T_0) - Q_0}{I(1 - 10^{-A_{808}})} = 60.1\%$$

Where $I$ is the laser lamp power ($I = 1\ W$), $A_{808}$ is the UV absorbance of the solution at 808nm ($A_{808} = 0.668$).
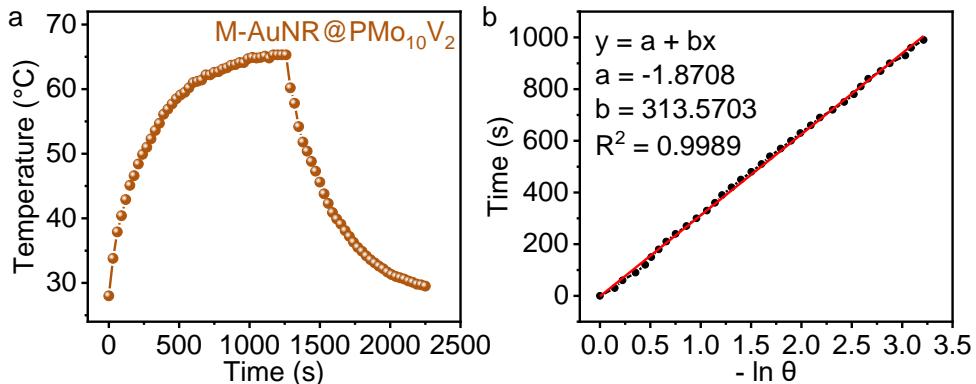


**Fig. S21.** (a) The temperature variation curve of M-AuNR@PMo$_{10}$V$_2$ in aqueous solution: the heating curve is the solution irradiated by the laser lamp (1W cm$^{-2}$), and the cooling process followed happens spontaneously at room temperature after turn off the lamp. (b) The plot of time versus the $-\ln(\theta)$ obtained from the cooling period.

**Calculation of the photothermal conversion efficiency of M-AuNR@Zn$_5$W$_{19}$.**

Calculation of the photothermal conversion efficiency ($\eta_{M-AuNR@Zn_5W_{19}}$)

$$\eta_{M-AuNR@Zn_5W_{19}} = \frac{hS(T_{Max} - T_0) - Q_0}{I(1 - 10^{-A_{808}})} = 65.5\%$$

14

Where $I$ is the laser lamp power ($I = 1\ W$), $A_{808}$ is the UV absorbance of the solution at 808nm ($A_{808} = 0.650$).
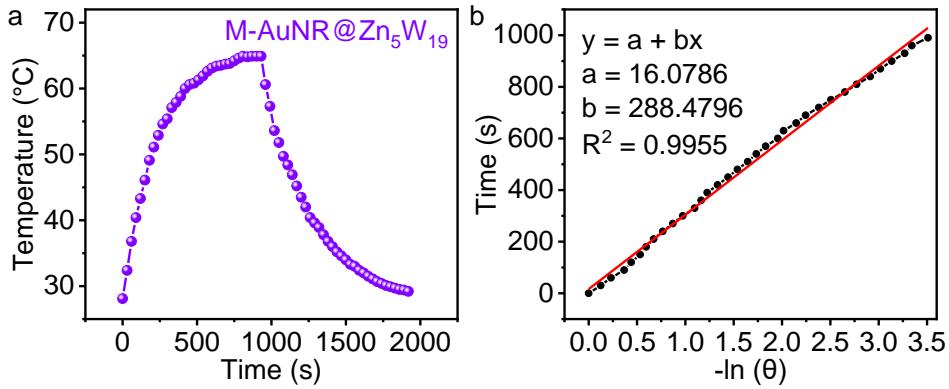


**Fig. S22.** (a) The temperature variation curve of M-AuNR@Zn$_5$W$_{19}$ in aqueous solution: the heating curve is the solution irradiated by the laser lamp (1W cm$^{-2}$), and the cooling process followed happens spontaneously at room temperature after turning off the lamp. (b) The plot of time versus the $-\ln(\theta)$ obtained from the cooling period.

**Calculation of the photothermal conversion efficiency of M-AuNR.**

Calculation of the photothermal conversion efficiency ($\eta_{M-AuNR}$)

$$\eta_{M-AuNR} = \frac{hS(T_{Max} - T_0) - Q_0}{I(1 - 10^{-A_{808}})} = 68.9\%$$

Where $I$ is the laser lamp power ($I = 1.0\ W$), $A_{808}$ is the UV absorbance of the solution at 808nm ($A_{808} = 0.759$).
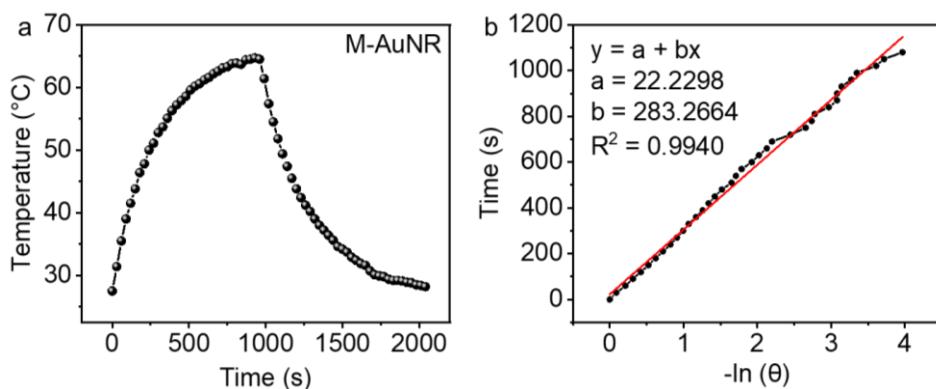


**Fig. S23.** (a) The temperature variation curve of M-AuNR in aqueous solution: the heating curve is the solution irradiated by the laser lamp (1W cm$^{-2}$), and the cooling process followed happens spontaneously at room temperature after turning off the lamp. (b) The plot of time versus the $-\ln(\theta)$ obtained from the cooling period.
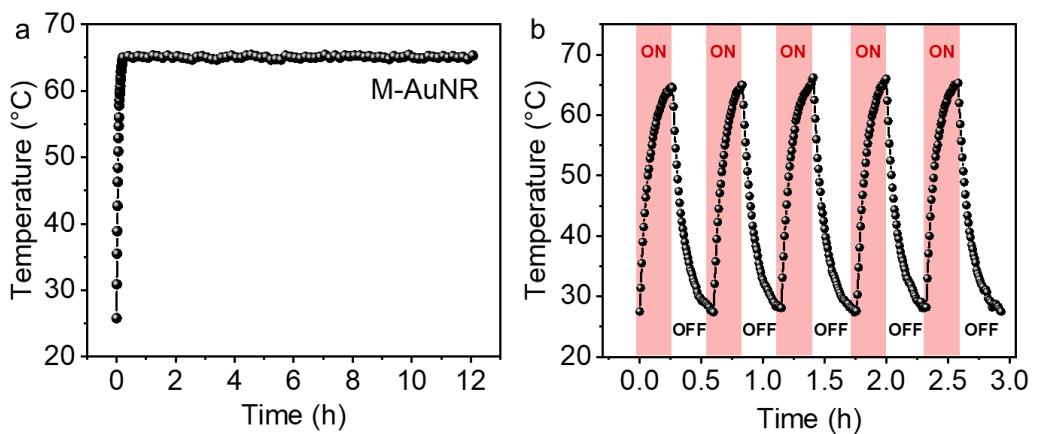
**Fig. S24.** The plots of temperature variation curves of M-AuNR in aqueous solution (a) under the continuous irradiation of the NIR laser lamp (1W cm$^{-2}$) and (b) over five cycles of laser on/off radiation.
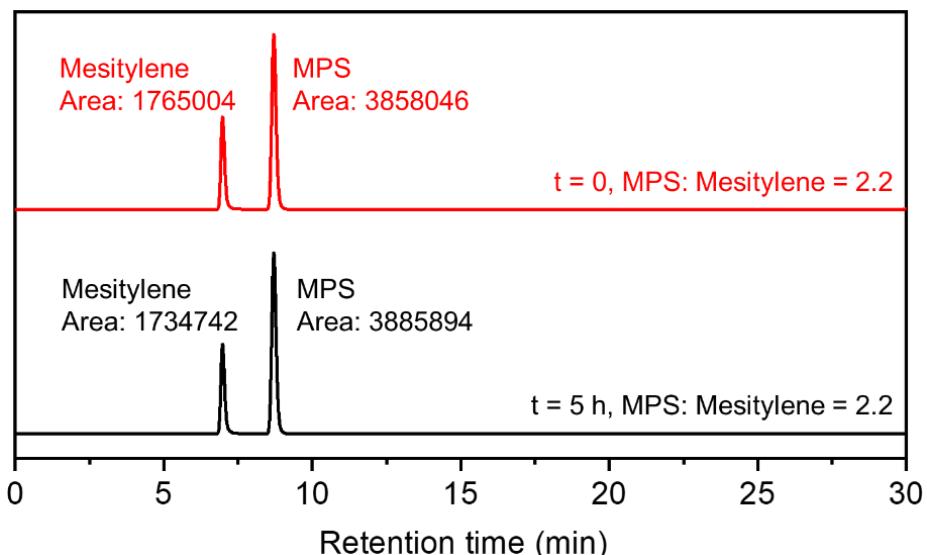


**Fig. S25.** Effect of M-AuNR on the concentration of MPS in aqueous solution recorded by HPLC. (0.16 mmol of MPS, 3.61 mmol of mesitylene as internal standard, in 1 mL M-AuNR aqueous solution, under the NIR laser irradiation at 65°C).

## S7. Photothermal catalytic data of M-AuNR@POM.
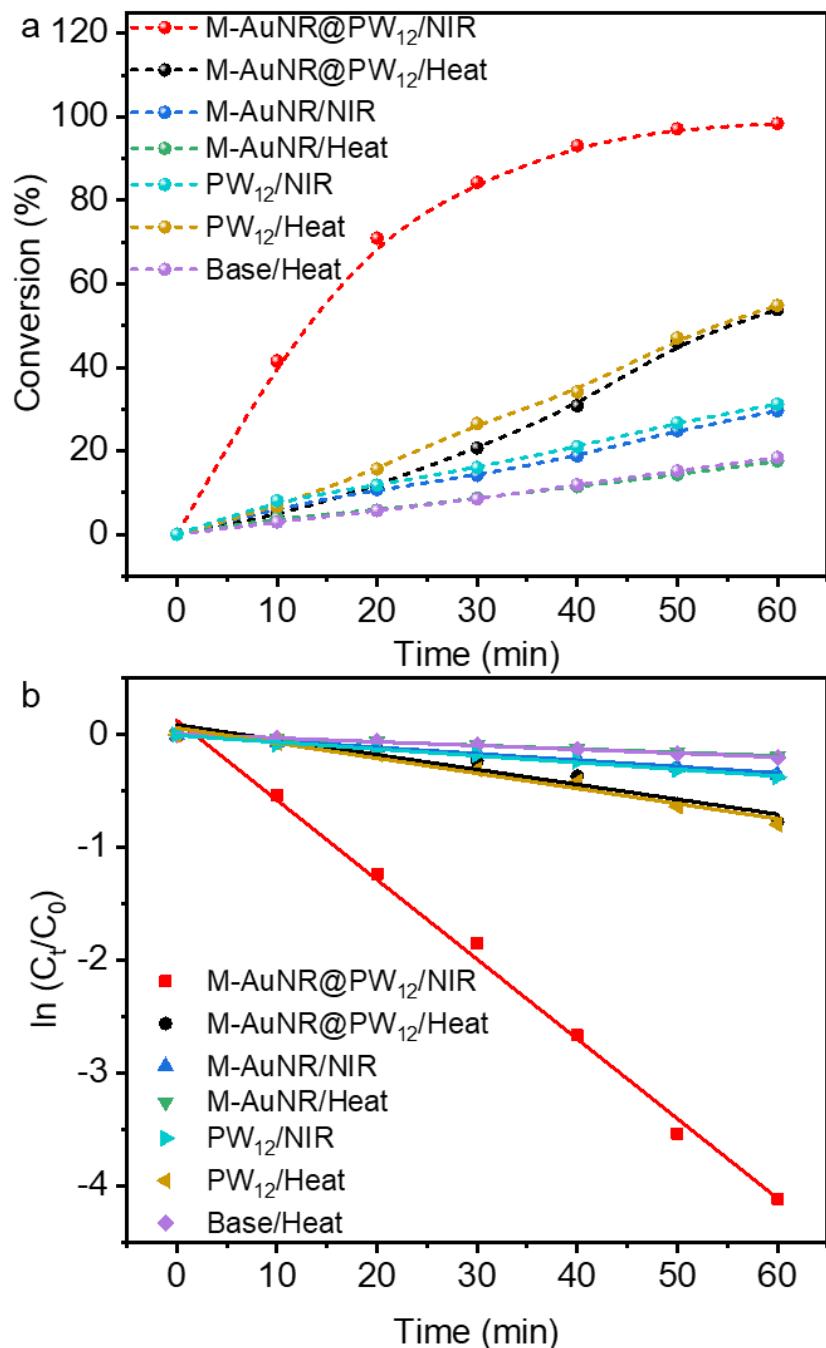


**Fig. S26.** (a) Conversion curves and (b) kinetic curves of MPS oxidation reaction catalyzed by different catalysts under NIR light irradiation (808 nm, 1W cm$^{-2}$) and heating condition. Reaction condition: 1mL catalyst aqueous solution (POMs: 19.9 ppm), substrate (0.16 mmol), $H_2O_2$ (1 equiv).
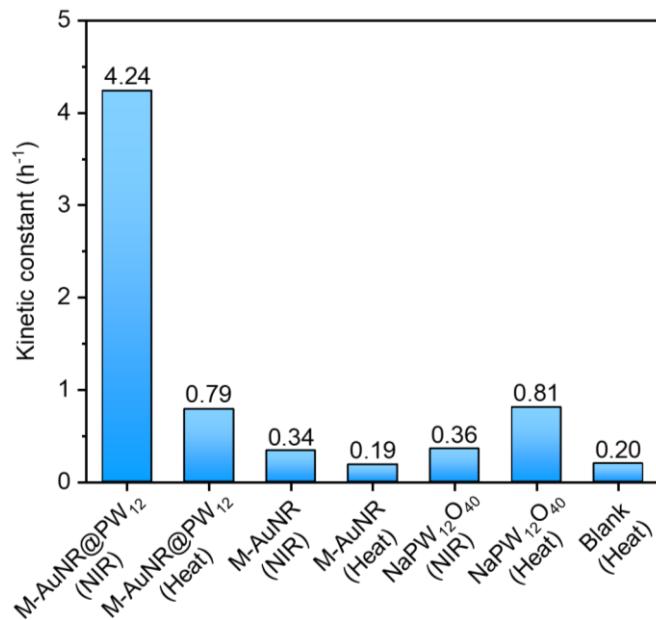
**Fig. S27.** Kinetic constant of MPS oxidation reaction catalyzed by different catalysts under NIR light irradiation (808 nm, 1.0 W cm$^{-2}$) and heating condition, in which reaction condition: 1.0 mL catalyst aqueous solution (POMs: 19.9 ppm), substrate (0.16 mmol), $H_2O_2$ (1 equiv).
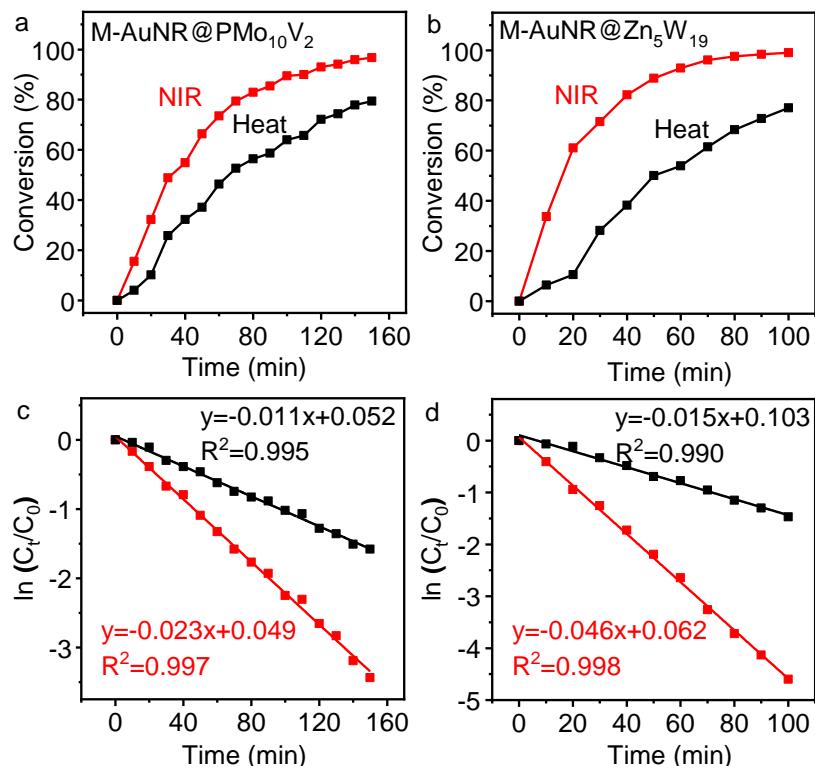


**Fig. S28.** The conversion curves of MPS oxidation reaction catalysed by (a) M-AuNR@PMo$_{10}$V$_2$ and (b) M-AuNR@Zn$_5$W$_{19}$ under NIR light irradiation (808 nm, 1W cm$^{-2}$) and heating condition. The kinetic curves of MPS oxidation reaction catalysed by (c) M-AuNR@PMo$_{10}$V$_2$ and (d) M-AuNR@Zn$_5$W$_{19}$ under NIR light irradiation (808 nm, 1W cm$^{-2}$) and heating condition. Reaction condition: 1mL catalyst aqueous solution, substrate (0.16 mmol), $H_2O_2$ (1 equiv).

18

**Table S1.** Results for the selective oxidation of MPS with $H_2O_2$ as the oxidant.



| Entry | Catalysts | Condition | Con./% | Sel./% A | Sel./% B | TOF/$h^{-1}$ | Ref |
|---|---|---|---|---|---|---|---|
| 1 | $Zn_4(Him)_2PMo_{12}$ | 10 min, 50°C, methanol | 99 | 99 | 1 | 1200 | 4 |
| 2 | $Co_3(H_2dpye)MnMo_9$ | 30 min, 50°C, methanol | 99 | 90 | 10 | 330 | 5 |
| 3 | ZnO-POM-HSNSs | 3 min, r.t, ethanol | 55.2 | 9.8 | 90.2 | 2535 | 6 |
| 4 | V-Ni-MOF | 60 min, 40°C, methanol | 100 | 99 | 1 | 20 | 7 |
| 5 | $Zn_2(C_{10}N_2H_8)PMo_{12}$ | 30 min, 50°C, methanol | 99 | 99 | 1 | 400 | 8 |
| 6 | $Zr_6B_2(\beta-SiW_{10})$ | 3 h, 80°C, acetonitrile | 86 | 22 | 78 | 57 | 9 |
| 7 | $Mn(TMR4A)Mo_6$ | 60 min, 40°C, methanol | 68 | - | - | 136 | 10 |
| 8 | $CuI_6(TPC4R-II)_3PMo_{12}$ | 3 h, 40°C, dichloromethane | 54 | - | - | 14 | 11 |
| 9 | $H_4PMo_{11}V \subset rho$-ZIF | 12 h, 25°C, methanol | 97 | 96 | 4 | 45 | 12 |
| 10 | $Ag-PW_{12}$ | 2 h, 20°C, n-octane | 100 | - | 100 | 261 | 13 |
| 11 | $PDDA-SiV_2W_{10}$ | 5 h, 25°C, water | 90 | 91 | 9 | 46 | 14 |
| **12** | **M-AuNR@PW$_{12}$** | **1 h, NIR, water** | **98.5** | **94.3** | **5.7** | **22785** | **This work** |
| **13** | **M-AuNR@Zn$_5$W$_{19}$** | **1 h, NIR, water** | **93.0** | **92.3** | **7.7** | **21523** | **This work** |
| **14** | **M-AuNR@PMo$_{10}$V$_2$** | **2 h, NIR, water** | **93.0** | **94.3** | **5.7** | **10756** | **This work** |
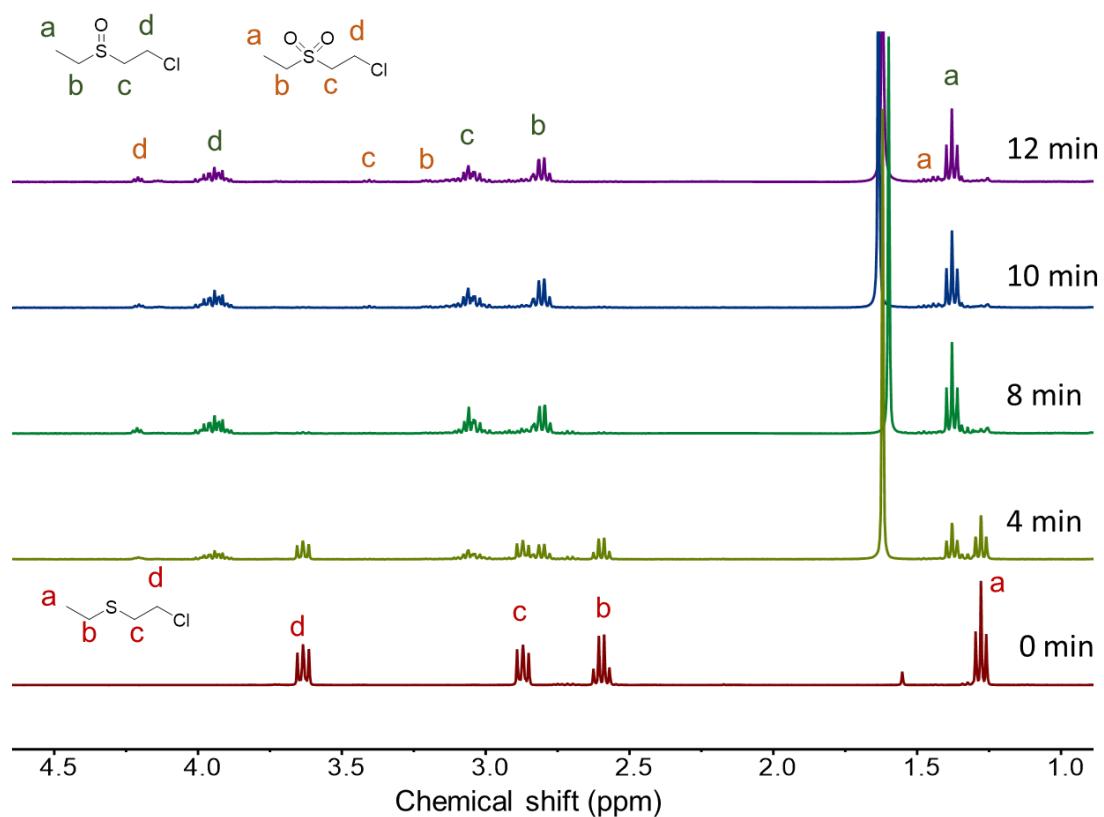
**Fig. S29.** NMR test experiment of CEES oxidation reaction catalyzed by M-AuNR@PW$_{12}$ under NIR light irradiation (808 nm, 1W cm$^{-2}$). Reaction condition: 1mL catalyst aqueous solution (POMs: 19.9 ppm), substrate (0.16 mmol), H$_2$O$_2$ (1 equiv).
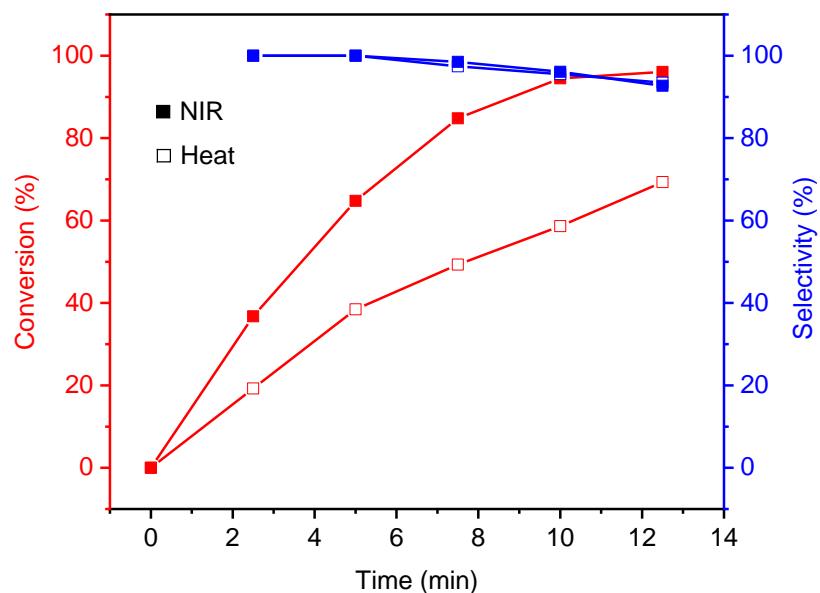


**Fig. S30.** The conversion and selectivity curves versus the time of CEES oxidation reaction catalyzed by M-AuNR@PW12 under NIR light irradiation (808 nm, 1W cm$^{-2}$) and heating conditions.

**Table S2.** Results for the selective oxidation of CEES with $H_2O_2$ as the oxidant.
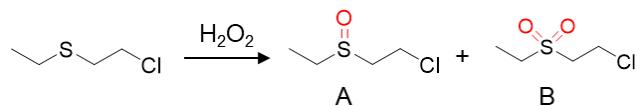


| Entry | Catalysts | Condition | Con./% | Sel./% | | TOF/h$^{-1}$ | Ref |
|---|---|---|---|---|---|---|---|
| | | | | **A** | **B** | | |
| 1 | PW12@ PIM-1-AO | 60 min, 45°C, acetonitrile | 100 | 86 | 14 | 50 | 15 |
| 2 | $B_{30}Gd_6$ $Ni_{12}Si_6W_{27}$ | 2 h, 60°C, acetonitrile | 96 | 97 | 3 | 45 | 16 |
| 3 | $Zn(Him)_2PMo_{12}$ | 10 min, r.t, methanol | 100 | 99 | 1 | 1200 | 4 |
| 4 | *om*-NENU-3a | 16 min, r.t, methanol | 100 | 99.8 | 0.2 | 469 | 17 |
| 5 | PMo$_{12}$@PDDA-rGO | 30 min, r.t, acetonitrile | 99 | 90 | 10 | 99 | 18 |
| 6* | $Ce_{12}V_6$-OTs | 100 min,30°C, acetonitrile | 99 | 99 | 1 | 28.2 | 19 |
| 7 | $V_6$-MOF | 40 min, r.t, ethanol | 100 | 100 | 0 | 30 | 20 |
| 8 | $Zn_2(C_{10}N_2H_8)$ $PMo_{12}$ | 30 min, r.t, methanol | 99 | 99 | 1 | 400 | 8 |
| 9 | $Mn(TMR4A)$ $Mo_6$ | 25 min, 40°C, methanol | 99 | 97 | 3 | 475 | 10 |
| 10 | $Ni(DTBA)_2V_2$ | 10 min, 40°C, methanol | 99 | 99 | 1 | 990 | 21 |
| 11 | V-Co-MOF | 10 min, r.t, ethanol | 100 | 100 | 0 | 60 | 22 |
| **12** | **M-AuNR @PW$_{12}$** | **10 min, NIR, water** | **94.5** | **96.1** | **3.9** | **131158** | **This work** |

* The oxidant is TBHP.

## S8. Photothermal catalytic stability measurements of M-AuNR@POM
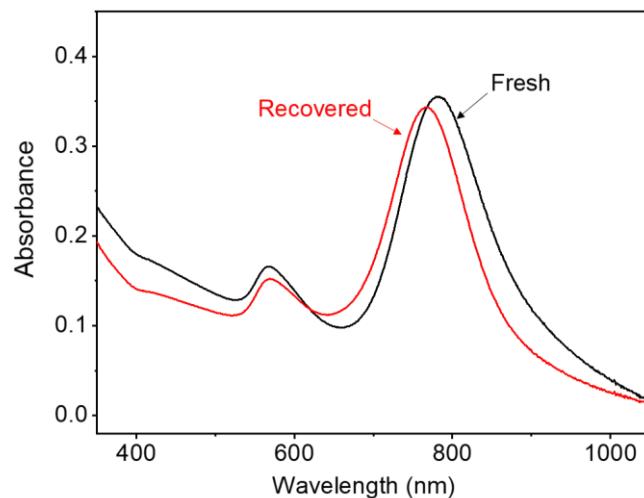


**Fig. S31.** The UV spectrum of freshed and recovered the M-AuNR@PW$_{12}$ after catalytic reaction.
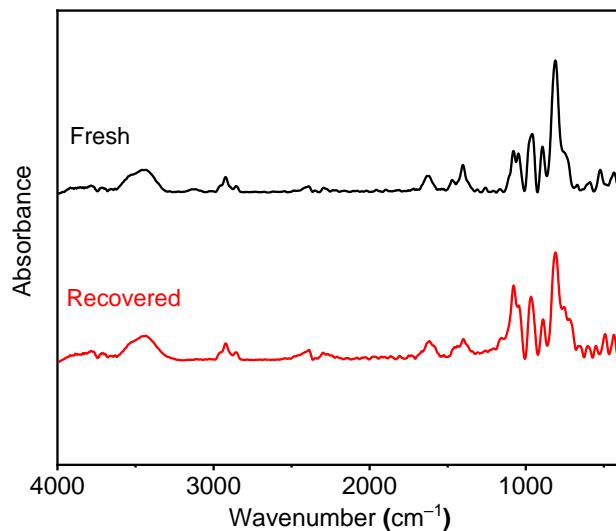


**Fig. S32.** The FTIR spectra of freshed and recovered the M-AuNR@PW$_{12}$.
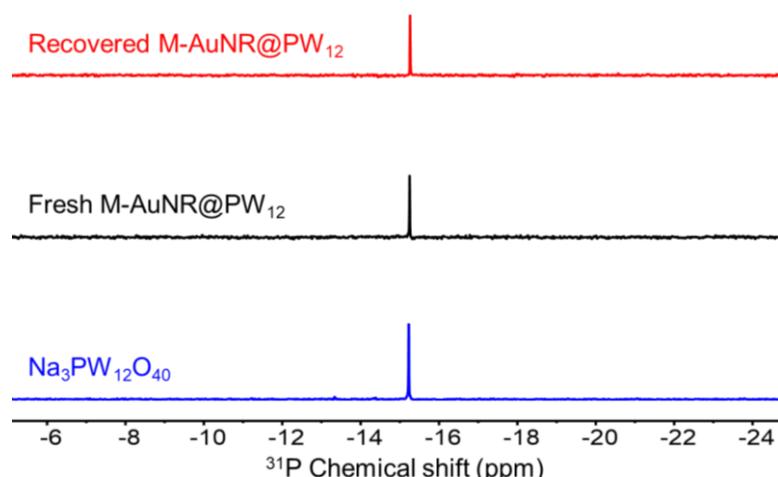


**Fig. S33.** $^{31}$P NMR spectrum of Na$_3$PW$_{12}$O$_{40}$, freshed M-AuNR@PW$_{12}$ and recovered M-AuNR@PW$_{12}$ in Methanol-$d_4$ at 25℃.
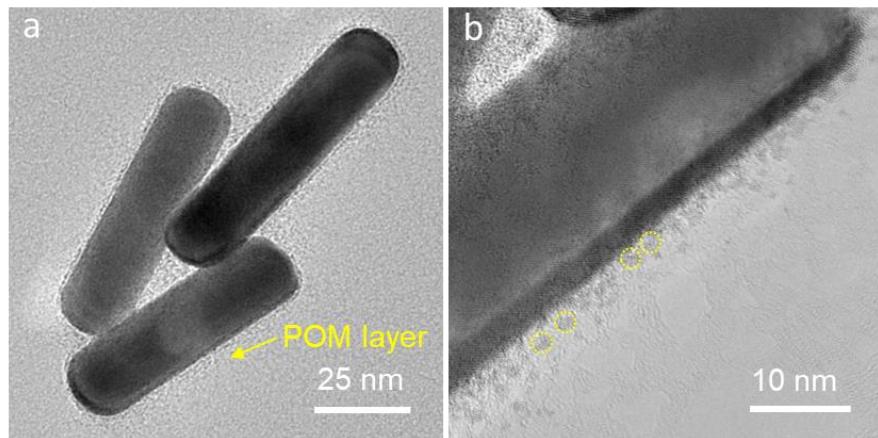
**Fig. S34.** TEM images of (a) recovered M-AuNR@PW$_{12}$ and (b) local magnification.
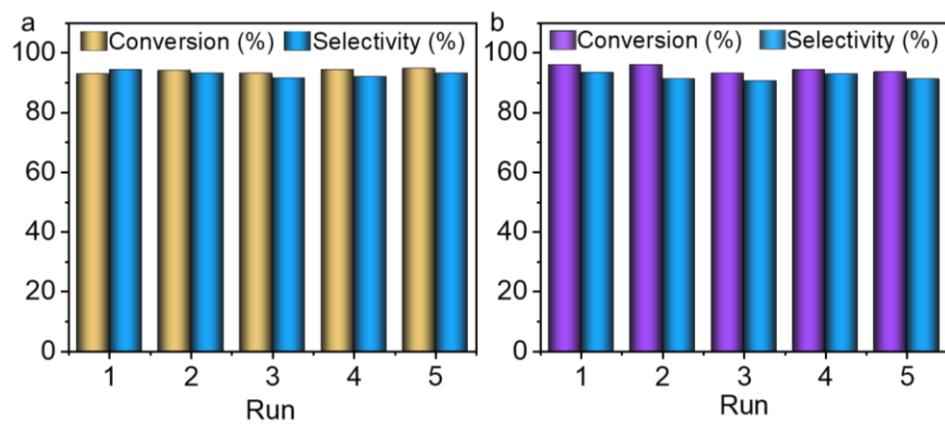


**Fig. S35.** Recycle test experiment of (a) M-AuNR@PMo$_{10}$V$_2$ and (b) M-AuNR@Zn$_5$W$_{19}$ in the selective oxidation of sulfide. Reaction condition: 1mL catalyst aqueous solution, substrate (0.16 mmol), H$_2$O$_2$ (1 equiv.).
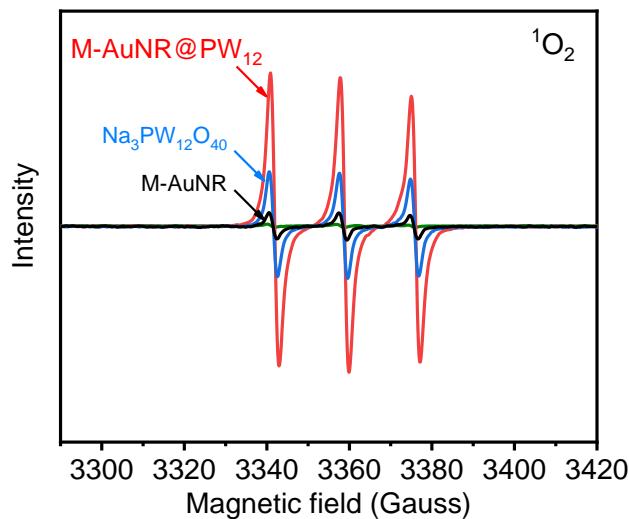


**Fig. S36.** EPR spectra of TEMP−$^1$O$_2$ generated in M-AuNR@PW$_{12}$ (red line), Na$_3$PW$_{12}$O$_{40}$ (external heating, blue line) and M-AuNR (black line) aqueous solution under NIR light irradiation for 20 min at 65°C.
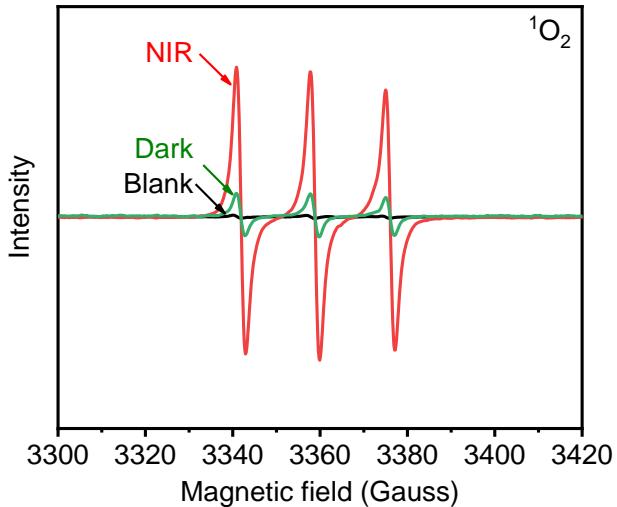
**Fig. S37.** EPR spectra of TEMP$-^1O_2$ generated in M-AuNR@PW$_{12}$ aqueous solution under NIR light irradiation (red line) and dark environment (green line) for 20 min at 65°C.
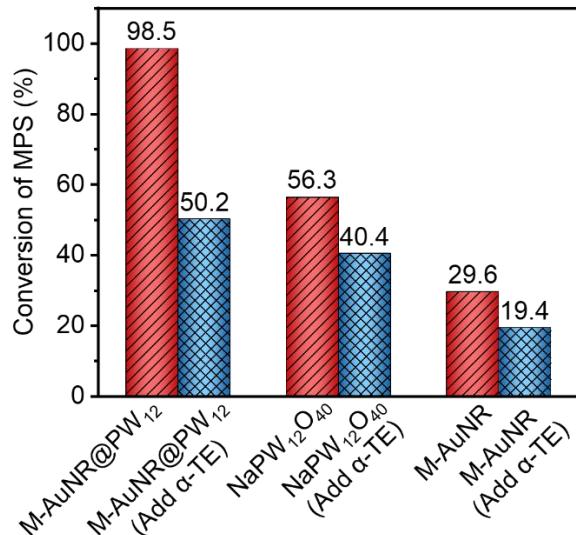


**Fig. S38.** Effect of α-TE (scavengers of $^1O_2$) on the photothermal catalytic oxidation of MPS. Reaction condition: 1mL catalyst aqueous solution, MPS (0.16 mmol), $H_2O_2$ (1 equiv), scavenger (1 equiv), under NIR light irradiation at 65°C (Na$_3$PW$_{12}$O$_{40}$ catalytic condition with external Heating).

## S9. Reference

1      G. A. Tsigdinos and C. J. Hallada, Molybdovanadophosphoric acids and their salts. I. Investigation of methods of preparation and characterization, *Inorg. Chem.*, 2002, **7**, 437–441.

2.     C. M. Tourné, G. F. Tourné and F. Zonnevijlle, Chiral polytungstometalates $[WM_3(H_2O)_2(XW_9O_{34})_2]^{12-}$ (X = M = Zn or CoII) and their M-substituted derivatives. Syntheses, chemical, structural and spectroscopic study of someD,Lsodium and potassium salts, *J. Chem. Soc., Dalton Trans.*, 1991, **1**, 143–155.

3.     J. M. Chalker, L. Lercher, N. R. Rose, C. J. Schofield and B. G. Davis, Conversion of cysteine into dehydroalanine enables access to synthetic histones bearing diverse post-translational modifications, *Angew. Chem. Int. Ed.*, 2012, **51**, 1835–1839.

4.     Y. Chen, H. An, S. Chang, Y. Li, Q. Zhu, H. Luo and Y. Huang, A POM-based porous supramolecular framework for efficient sulfide–sulfoxide transformations with a low molar O/S ratio, *Inorg. Chem. Front.*, 2022, **9**, 3282–3294.

5.     Q. Liu, H. Lin, X.-L. Wang, X. Wang, N. Xu, Y. Tian, L. Yang, X. Li and J. Sun, Two novel polyoxometalate-based metal–organic complexes with chiral Waugh-type $[MnMo_9O_{32}]^{6-}$ anions as high-efficiency catalytic oxidative desulfurization catalysts, *Cryst. Growth Des.*, 2021, **21**, 7015–7022.

6.     J. Liu, W. Shi and X. Wang, ZnO-POM cluster sub-1 nm nanosheets as robust catalysts for the oxidation of thioethers at room temperature, *J. Am. Chem. Soc.*, 2021, **143**, 16217–16225.

7.     T.-Y. Dang, R.-H. Li, H.-R. Tian, Q. Wang, Y. Lu and S.-X. Liu, Tandem-like vanadium cluster chains in a polyoxovanadate-based metal–organic framework for efficient catalytic oxidation of sulfides, *Inorg. Chem. Front.*, 2021, **8**, 4367–4375.

8.     Y. Chen, S. Chang, H. An, Y. Li, Q. Zhu, H. Luo and Y. Huang, Two polymorphic polyoxometalate-based metal–organic frameworks for the efficient synthesis of functionalized sulfoxides and detoxification of mustard gas simulants, *ACS Sustainable Chem. Eng.*, 2021, **9**, 15683–15693.

9.     Z. Zhang, Y. L. Wang, Y. Liu, S. L. Huang and G. Y. Yang, Three ring-shaped Zr(iv)-substituted silicotungstates: syntheses, structures and their properties, *Nanoscale*, 2020, **12**, 18333-18341.

10.    M. Y. Yu, J. Yang, T. T. Guo and J. F. Ma, Efficient catalytic oxidative desulfurization toward thioether and sulfur mustard stimulant by polyoxomolybdate-resorcin[4]arene-based metal-organic materials, *Inorg. Chem.*, 2020, **59**, 4985–4994.

11.    Y. L. Xiong, M. Y. Yu, T. T. Guo, J. Yang and J. F. Ma, A nanosized Propeller-like polyoxometalate-linked copper(I)-resorcin[4]arene for efficient catalysis, *Inorg. Chem.*, 2020, **59**, 15402–15409.

12.    X. Zhao, Y. Duan, F. Yang, W. Wei, Y. Xu and C. Hu, Efficient mechanochemical synthesis of polyoxometalate subsetZIF complexes as reusable catalysts for highly selective oxidation, *Inorg. Chem.*, 2017, **56**, 14506–14512.

13.    H. Zhang, X. Xu, H. Lin, M. A. Ud Din, H. Wang and X. Wang, Silver nanocrystal-decorated polyoxometalate single-walled nanotubes as nanoreactors for desulfurization catalysis at room temperature, *Nanoscale*, 2017, **9**, 13334–13340.

14.    W. Zhao, C. Yang, Z. Cheng and Z. Zhang, A reusable catalytic system for sulfide oxidation and epoxidation of allylic alcohols in water catalyzed by poly(dimethyl diallyl) ammonium/polyoxometalate, *Green Chem.*, 2016, **18**, 995–998.

15.	D. Jung, S. Su, Z. H. Syed, A. Atilgan, X. Wang, F. Sha, Y. Lei, N. C. Gianneschi, T. Islamoglu and O. K. Farha, A catalytically accessible polyoxometalate in a porous fiber for degradation of a mustard gas simulant, *ACS Appl. Mater. Interfaces*, 2022, **14**, 16687–16693.

16.	Y. Chen, Z.-W. Guo, X.-X. Li, S.-T. Zheng and G.-Y. Yang, Multicomponent cooperative assembly of nanoscale boron-rich polyoxotungstates with 22 and 30 boron atoms, *CCS Chem.*, 2022, **4**, 1305–1314.

17.	Z. Zhang, Y. Liu, H. Tian, X. Ma, Q. Yue, Z. Sun, Y. Lu and S. Liu, Hierarchically ordered macro-microporous polyoxometalate-based metal-organic framework single crystals, *ACS Nano*, 2021, **15**, 16581–16588.

18.	Y. Wu, J. Dong, C. Liu, X. Jing, H. Liu, Y. Guo, Y. Chi and C. Hu, Reduced polyoxomolybdate immobilized on reduced graphene oxide for rapid catalytic decontamination of a sulfur mustard simulant, *Dalton Trans.*, 2021, **50**, 9796–9803.

19.	X. Wang, K. Brunson, H. Xie, I. Colliard, M. C. Wasson, X. Gong, K. Ma, Y. Wu, F. A. Son, K. B. Idrees, X. Zhang, J. M. Notestein, M. Nyman and O. K. Farha, Heterometallic Ce$^{IV}$/V$^{V}$ oxo clusters with adjustable catalytic reactivities, *J. Am. Chem. Soc.*, 2021, **143**, 21056–21065.

20.	H. R. Tian, Z. Zhang, T. Y. Dang, S. M. Liu, Y. Lu and S. X. Liu, Hollow Lindqvist-like-shaped {V$_6$} cluster-based metal-organic framework for the highly efficient detoxification of mustard gas simulant, *Inorg. Chem.*, 2021, **60**, 840–845.

21.	X. Wang, T. Zhang, Y. Li, J. Lin, H. Li and X. L. Wang, In situ ligand-transformation-involved synthesis of inorganic-organic hybrid polyoxovanadates as efficient heterogeneous catalysts for the selective oxidation of sulfides, *Inorg. Chem.*, 2020, **59**, 17583–17590.

22.	H.-R. Tian, Z. Zhang, S.-M. Liu, T.-Y. Dang, X.-H. Li, Y. Lu and S.-X. Liu, A novel polyoxovanadate-based Co-MOF: Highly efficient and selective oxidation of a mustard gas simulant by two-site synergetic catalysis, *J. Mater. Chem. A*, 2020, **8**, 12398–12405.